ANNALS OF GEOPHYSICS, 67, 6, S659, 2024; doi:10.4401/ag-9095
OPEN ACCESS

Crustal and uppermost mantle shear-wave velocity structure beneath the Northeastern Iranian Plateau using an analysis of receiver function and surface-wave tomography

Fatemeh Roostaee[1], Gholamreza Mortezanejad[2], Habib Rahimi[*,1], Ali Gholami[3]

(1) Institute of Geophysics, University of Tehran, Tehran, Iran
(2) School of Earth Sciences, Damghan University, Damghan, Iran
(3) Institute of Geophysics, Polish Academy of Sciences, Warszawa, Poland

Article history: received April 4, 2024; accepted February 2, 2025

Abstract

In this study, we investigate the crustal velocity structure and Moho discontinuity depth beneath the NE Iran continental collision zone through joint inversion of P receiver function and Rayleigh wave group velocity dispersion curves. Local Rayleigh wave group velocity dispersion curves were estimated using time-frequency analysis method and two-dimensional surface wave tomography method. Our results distinctly highlight prominent changes in velocity structure along both the northern and southern flanks of Daruneh fault, occurring at both the crustal and lithospheric scales. This fault boundary can consequently be characterized as a microplate demarcation. In addition, our analysis indicates that variations in the average thickness of low-velocity layers within the upper crust and sedimentary cover are distinguishable between central Iran and the Kopeh Dagh and Binalud mountain ranges. We think that the greater thickness of low-velocity layers beneath Kopeh Dagh and Binalud is caused by the convergence of the Iran and Turan plates, the presence of thickened sedimentary layers, mountainous terrain, and folded sedimentary structures in these areas. Our study reveals that the South Caspian Basin has a distinct crust and lithosphere compared to its surrounding area in the northeast of Iran. Our results reveal some evidence indicating that the Kashafrud reverse fault between Binaloud and Kopeh Dagh mountains is the suture line of the closed Palaeotethys Ocean. We also found the maximum and minimum values for Moho depth beneath Kopeh Dagh mountain range (~56 km) and Central Iran microplate (~32 km), respectively.

Keywords: P receiver functions; Surface wave tomography; Shear wave velocity structure; Kopeh Dagh; Iranian Plateau

1. Introduction

The Iranian Plateau is a vast region located between the Arabian and Eurasian plates, experiencing deformations due to the northward motion of the Arabian shield relative to the Eurasian plate at a rate of approximately 22 mm/y (Vernant et al., 2004). This convergence leads to closure of Palaeotethys and Neotethys Oceans and formation of significant mountain ranges named Zagros, Alborz, and Kopeh Dagh (KD) through the processes of shortening and thickening along different faults systems which are part of the Alpine-Himalayan orogeny, as well as the formation of the shear zones around the rigid Central Iran (CI) microplate (Jackson and McKenzie, 1984).

In this study, we define Northeastern (NE) Iran as the region bounded by latitudes 33.5° to 38.5° N and longitudes 55° to 61° E (Fig. 1). This area contains the northern part of the CI microplate in the south and southeast, the Eastern Alborz (EALB) Mountain range and the southeastern part of South Caspian Basin (SCB) in the northwest, and the KD and Binalud (BL) mountain ranges in the north. Although studying the structure of the crust and upper mantle in NE Iran is of vital importance due to high seismicity, dense population, and complex tectonic regimes, this area is significantly underexplored compared to other regions of the Iranian Plateau. On the other hand, some aspects of the structure of the crust and upper mantle as well as the boundary of the main tectonic zones in NE Iran are still unclear or under debate. The result of this study would be more helpful in answering the questions about these aspects. For example; How does the SCB interact with its surrounding area in the scale of crust and upper mantle in NE Iran? Can we find any evidence of the Palaeotethys suture zone in NE Iran? Is there any significant discontinuity in the velocity structure of the crust and upper mantle in the boundary of CI microplate with its surrounding areas in the north? How is the lateral variation of the low velocity layers of the upper crust in NE Iran? How is the Moho depth distribution across different tectonic units in NE Iran?

In this study, we used a comprehensive approach to investigate the crust and upper mantle velocity structure beneath the NE Iran continental collision zone. This study involved three main components. First, we applied a two-dimensional (2D) surface wave tomography method to analyze the fundamental mode of Rayleigh waves recorded by broadband seismic stations in the region. This involved gridding the region into cells and obtaining Rayleigh wave group velocity dispersion curves for each cell using tomographic images. Second, we calculated P receiver functions to determine the detailed shear wave velocity structure beneath the seismic stations. Finally, the obtained Rayleigh wave dispersion curves and P receiver functions were jointly inverted beneath each seismic station using the “joint 96” program in the CPS software package (Herrmann and Ammon, 2007; Herrmann, 2013). This technique leverages the weighted damped least squares method to produce one-dimensional (1D) velocity models at different depths beneath each station (Julia et al., 2000). The integration of these methods allowed for a robust and detailed characterization of the subsurface geological features in this tectonically active region.

2. Tectonic and Geological setting

NE Iran plays a key role in accommodating or transferring deformation resulting from the convergence and collision between the CI and the Turan (TR) platform (Fig. 1). The ophiolite deposits found in BL (Fig. 1) are considered remnants of this tectonic collision after closure of the Palaeotethys ocean, which began during the Middle Triassic and ended in the Late Triassic (Berberian, 1981; Sengor 1984; Sengor et al., 1988). The current convergence rate between the CI and TR is estimated at approximately 6 mm per year (Vernant et al., 2004). In this area, a 600 km long and 200 km wide expanse of mostly parallel mountain ranges, specifically KD and BL ranges, has formed (Mirzaei et al., 1998). In the northeast, the KD range marks the primary deformation zone associated with the Arabia-Eurasia collision and serves as the boundary between the CI and the TR (Shabanian et al., 2009a and 2009b). It is tectonically demarcated from the TR platform by a southward-thrusting fault (Hollingsworth et al., 2009), which is believed to be the eastern segment of the right-lateral strike-slip Ashkabad Fault (ASF; see Fig. 1). The KD range extends from the northwest to the Absheron Ridge, delineating the northern boundary of the SCB (Brunet et al., 2003). The eastern border of the KD range is situated around 60°E, where seismicity significantly decreases. This border separates the non-seismic zone of western Afghanistan from the seismic zone of the KD, although its structural characteristics remain unclear. (Mirzaei et al., 1998).

The KD features a Mesozoic-Tertiary sedimentary cover with an approximate thickness of 10 km, which underwent folding during the late stages of the Alpine orogeny (Davoudzadeh et al., 1984; Zonenshain et al., 1990; Maksimov, 1992; Brunet et al., 2003). Recent GPS measurements have revealed variable deformation characteristics along

KD, with its southeastern part characterized by predominantly low-rate thrust faulting and its northwestern part exhibiting mostly high-rate strike-slip activity (Masson et al., 2007). The uplift of KD is primarily driven by a fold-fault strip, featuring northward thrusting in the north and southward thrusting in the south. These geological observations are supported by analyses of earthquake focal mechanisms along the northern margin (e.g., the October 5, 1948 earthquake in Ashkabad) and the southern margin (e.g., the March 21, 1963 earthquake in Esfrain) (Berberian, 1981).

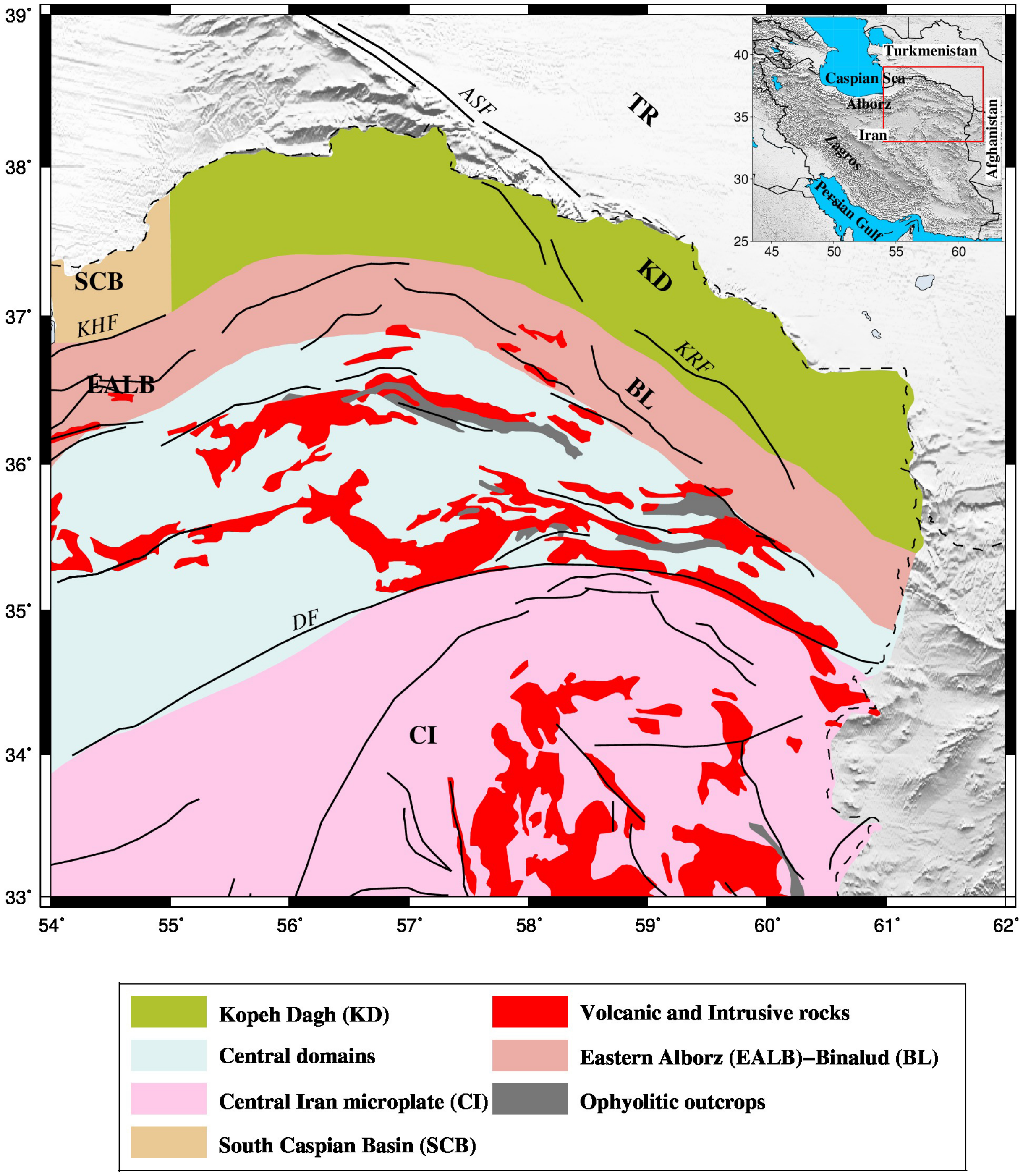

Figure 1. Tectonic units of NE Iran. Solid lines indicate the major active faults, modified from Hessami et al. (2003). A large-scale map of the region is plotted on the top right corner. Abbreviations of major active faults shown by italic acronyms: ASF, Ashkabad Fault; KHF, Khazar Fault; KRF, Kashafrud reverse fault; DF, Doruneh Fault. Abbreviations of main tectonic units shown by bold acronyms: BL, Binalud mountain range; KD, Kopeh Dagh mountain range; CI, Central Iran microplate; SCB, South Caspian Basin; EALB, Eastern Alborz Mountain range; TR, Turan platform.

The BL Mountain range, located to the south of the KD range can be considered an eastern extension of the Eastern Alborz (EALB) mountains (Alavi, 1992). The boundary between the BL and KD mountains is delineated by a narrow sedimentary basin known as the Atrak-Kashafrud line, which runs closely parallel to the Kashafrud Reverse Fault (KRF; see Fig. 1). Alavi (1996) posits that the KRF marks the suture between the Iranian Plateau and the Eurasian Plate after closure of Palaeotethys ocean; however, some studies (e.g., Stampfli et al., 2001) continue to depict the ASF as the suture zone. Despite the southern border of KD range, the southern border of BL range does not exhibit any significant geological structures.

The Doruneh Fault (DF) is a major geological feature that extends approximately 900 km across the Iranian plateau. It is recognized as the northern boundary of the CI microplate. (Wellman, 1965; Stocklin et al., 1973; Javadi et al., 2013; Tadayon et al., 2019). The CI microplate is characterized by a complex mosaic of smaller rigid tectonic blocks that are separated by right-lateral strike-slip faults (Berberian et al., 1981; Tirrul et al., 1983; Soffel et al., 1996; Aghanabati, 2004). The DF is demarcated into three distinct segments with different fault systems. The western part of DF exhibits a reverse left-lateral mechanism with a left-handed step-over geometry while in the central part of DF, the fault mechanism is purely left-lateral strike-slip, featuring nearly parallel faults and the eastern part of DF encompasses a complex network of at least fifteen NE-dipping reverse faults (Javadi et al., 2013; Farbod et al., 2011).

The current crust and upper mantle structure of NE Iran is a product of the ongoing Arabian-Eurasian continental collision. Several independent studies have investigated crustal thickness in this region (Rahimi et al. 2014; Nowrouzi et al. 2007; Shadmanaman et al. 2010; Taghizadeh-Farahmand et al. 2013), revealing an average thickness ranging from ~27 km beneath the CI to ~55 km beneath the KD and BL ranges. Motaghi et al. (2012, 2014) using receiver function and surface wave dispersion curve data, found evidence of crustal thickening up to 55 km beneath BL foreland basin, which can be interpreted as an indication of the thrusting of the Eurasian plate beneath the Iranian plateau. Regarding lithospheric structure, it appears that there is a relatively thin continental lithosphere, measuring approximately 85-95 km beneath the KD range (Taghizadeh-Farahmand et al. 2013).

The South Caspian Basin (SCB), located to the north of Iran, is separated from its southern surrounding areas by the Khazar Fault (KHF; see Fig. 1). This rigid block significantly influences the crustal and upper mantle structures of its adjacent regions. The SCB is considered to be a remnant of a larger back-arc basin associated with Tethyan subduction (e.g., Brunet et al., 2003) and is thought to possess a relatively thick (~13 km) and high-velocity oceanic-like crust, underpinned by extremely thick (~20 km) low shear wave velocity sediments (Brunet et al., 2003; Knapp et al. 2004). Regarding the lithospheric structure of SCB, it has been suggested that it features a thick, rigid and high velocity mantle lid (e.g., Mortezanejad et al. 2019; Al-Lazki et al. 2003; 2004; 2014).

3. Methodology

Analyzing the lateral variations of group velocity of dispersion curves offers valuable insights into the velocity structure of a region, aiding investigations into tectonic and geological units. The 2D surface wave tomography is a method that utilizes phase and group velocities at a certain period extracted from calculated dispersion curves of a range of event-station paths and computes phase and group velocity values for that period in any point within the study area. These values enable us to plot tomographic maps for the selected period. Doing the tomography for a range of periods, enables us to make a dispersion curve at any point within the study area. Such dispersion curves are used to study the depth and lateral variation of shear wave velocity in the region by inverting them. Individual inversion of the dispersion curve, cannot accurately determine velocity discontinuities because surface wave dispersion curves are more sensitive to average shear wave velocity rather than velocity contrast of discontinuities. To solve this challenge, joint inversion of dispersion curves with other independent data sets, such as P receiver function, is widely employed (e.g., Julia et al., 2000).

The Yanovskaya-Ditmar method is a widely used approach for generating 2D tomography maps of group velocities (Yanovskaya et al., 1990; Ditmar et al., 1987; Yanovskaya, 1997). This method aims to minimize the differences between observed travel times and those predicted by a velocity structure model. The optimization process involves minimizing the function:

$$(d - Gm)^T (d - Gm) + \alpha \iint |\nabla m(x)|^2 dx \rightarrow min$$

where

$$d_i = (t_i - t_{i0})$$

$$m(x) = \left(V^{-1} - {V_0}^{-1}\right)V_0$$

$$(Gm)_i = \iint G_i(x)m(x)dx = \int_{l_{i0}} m(x)\frac{ds}{V_0}$$

$$\iint G_i(x)dx = \int_{l_{i0}} \frac{ds}{V_0} = t_{i0}$$

Where the variable d represents input data indicating travel time residuals along ith ray path, G denotes the data kernel associated with the initial model and α serves as a regularization parameter that controls the balance between data fitting and velocity maps smoothness. ∇m denotes the gradient of the model, and di, $Gi(x)$, and V_0 correspond to observed travel time residual, the kernel associated with the initial model, and initial group velocity values, respectively. t_i denotes observed travel time along the ith path, t_{i0} represents calculated travel time for the initial model, l_{i0} denotes the length of the i$^{\text{th}}$ path, and s is the length of the section over which the inversion is conducted.

In addition to the ray coverage and estimated errors, the tomography method employed in this study incorporates two more important parameters for controlling the quality of tomography results. The 1st and most important parameter known as the length of 'averaging area', denoted as L, which serves as a measure of data resolution power at each point and controls the stability and reliability of the tomography results (Yanovskaya et al., 1998). In other words, this parameter is like a checkerboard test that is usually used in tomographic studies (Yanovskaya et al., 1990; Ditmar et al., 1987; Yanovskaya, 1997). The value of L is determined by the density of ray paths within each cell of the study area. Smaller values of L indicate higher resolution power, which is a result of a higher density of ray paths crossing through that area. Conversely, larger values of L correspond to lower resolution power. The resolution varies at each point due to differences in path density and orientation, crucial for estimating the smallest detectable heterogeneity size via inversion methods. Specifically, the averaging area is determined using the relationship $L = [\mathrm{Smax(x, y)} + \mathrm{Smin(x, y)}]/2$, where Smax and Smin represent the larger and smaller axes of the ellipse centered at point (x,y), respectively.

The 2nd parameter introduced by the tomography method for controlling the quality of tomography results is known as 'stretching,' which is calculated as $\mathrm{E} = 2[\mathrm{Smax(x, y)} - \mathrm{Smin(x, y)}]/[\mathrm{Smax(x, y)} + \mathrm{Smin(x, y)}]$. This parameter evaluates the heterogeneities in ray parameters. The value E is dimensionless and varies between 0 and 2. A value of zero indicates that Smax(x, y) equals to Smin(x, y), resulting in the transformation of the ellipse to a circle, which implies uniform azimuthal coverage of ray paths. This uniformity is crucial because it suggests that the seismic collected data provide a balanced representation of subsurface properties from all directions, leading to more reliable imaging. Conversely, if Smax(x, y) is significantly larger than Smin(x, y), E approaches 2 (Yanovskaya, 1997). In this case, the ellipse becomes highly elongated, indicating that all ray paths have a clear preferred orientation. This scenario is problematic because it suggests that the data may be biased toward certain directions, resulting in poor resolution and limited ability to accurately characterize subsurface structures. Such directional bias can lead to gaps in information and misinterpretations of geological features. Mapping the stretching parameter is essential for assessing the quality and reliability of tomographic models. Understanding the implications of ray path orientations helps researchers identify areas where additional data collection may be necessary to improve resolution and reduce bias in subsurface imaging.

In investigating the Earth's interior structure, the receiver function method plays a crucial role. Receiver functions are sensitive to shear wave velocity contrasts at various interfaces within the medium, as well as to the relative travel times of converted waves that reverberate between these interfaces. This sensitivity allows for the identification of seismic discontinuities, which is essential for defining the Earth's structure. However, it is important to note that interpretations of receiver function data may exhibit an apparent depth-velocity trade-off (Ammon et al. 1990). In contrast, single-mode surface wave dispersion curves provide constraints on average absolute shear wave velocities across different depth ranges. Therefore, the joint interpretation of surface wave dispersion curves and receiver functions can yield more robust constraints on shear wave velocity structures than either technique could provide independently. The theory behind receiver function method has been extensively documented in various studies (e.g., Langston (1979); Owens et al. (1984); Kind et al. (1988); Ammon et al. (1990); Ammon (1991) and Vinnik (1977)). Here we try to review this method briefly. The recorded waveforms at each station contains vital information about the earthquake source, propagation effects – including those from near-source and deep structures – and characteristics of the recording device. By applying the receiver function method, we can effectively isolate and remove the effects of the source, near source and deep structures, and the recording device from the observed waveform of each station; thus, what remains is a representation of the Earth's structure beneath the station, referred to as the "receiver function". To obtain receiver function we can use the waveform of teleseismic or regional earthquakes, recorded by three-component seismic stations. The first step in obtaining receiver function at a specific seismic station is removing the mean, trend and filtering of the waveform to remove the very long period undulation. After that, we should remove the instrument responses for each component of the waveform. The next step is rotating the waveform from ZNE coordinated to ZRT. The final step is removing the effect of source of event and propagation path from the R component of the waveform using the iterative deconvolution method in the time domain (Ligorria and Ammon, 1999) or deconvolution method in the frequency domain (Langston 1979). The final R component at this stage is called P receiver function. This time series contains the converted phases (Ps) and multiples (PpPs, PsPs, PpSs, ...) produced by the velocity discontinuities beneath the station. The receiver function method has been extensively used by researchers such as Langston (1979), Owens et al. (1984), Kind et al. (1988), Ammon et al. (1990), Ammon (1991), Mangino et al. (1993), Kind et al. (1995), Sheehan et al. (1995), Vinnik (1977), Kosarev et al. (1999), Zhu et al. (2000), Sodoudi (2005). One of the methods to extract information from receiver functions is to invert them to a 1D shear wave velocity model beneath the station. It is important to note that the inversion of receiver functions involves a trade-off between depth and shear wave velocity, potentially leading to non-unique solutions. Particularly, inaccuracies in estimating P-wave and especially S-wave velocities can significantly influence the determination of discontinuity depths and velocity of layers (Ammon, 1991). In fact, the receiver functions are more sensitive to the velocity contrast of discontinuities rather than the average shear wave velocity of the layers. This trade-off highlights a limitation of receiver functions in accurately resolving subsurface structures. However, the ambiguity due to this trade-off might be resolved by considering other independent data.

The joint inversion method of the receiver functions and surface wave dispersion curves is a powerful approach for determining the structure of the Earth beneath a given receiver station. This method combines two independent sets of physical data-receiver functions and dispersion curves from surface waves- to overcome the limitations of individual methods and produce a more accurate and higher quality 1D velocity model of the subsurface.

In the joint inversion method for receiver function and surface wave dispersion curves, two independent data sets are utilized and combined using the weighting parameter P. The goal of the iterative process is to minimize the error value in relation to the observed and predicted data components in order to obtain a model that closely represents the true model. The error function, denoted as E, is given by the following equation:

$$E = \frac{(1-P)}{N_r}\sum_{i=0}^{N_r}\left(\frac{O_{ri}-P_{ri}}{\sigma_{ri}}\right)^2 + \frac{P}{N_s}\sum_{j=0}^{N_s}\left(\frac{O_{sj}-P_{sj}}{\sigma_{sj}}\right)^2$$

where P is the weighted influence parameter, O_{ri} is the i^{th} data point of the observed receiver function, P_{ri} is the i^{th} data point of the predicted receiver function, σ_{ri} is the standard error of the i^{th} data point of the receiver function, O_{sj} is the observed dispersion curve in the j^{th} data point, P_{sj} is the predicted dispersion curve in the j^{th} data point, and σ_{sj} is the standard error of the j^{th} data point of the observed dispersion curve. Nr and Ns represent the number of receiver function and dispersion curve data points, respectively. The coefficients 1/Nr and 1/Ns are used to remove the effect of different numbers of data points of the observed receiver function and the dispersion curve in the inversion process.

4. Data

In this study our database comprises two distinct datasets. The first is the dataset for dispersion curve tomography and the second is the dataset for receiver function analysis. To build our dataset for surface wave analysis, we used

284 local and regional earthquakes (Fig. 2) that occurred in NE Iran between 2012 and 2018, with magnitudes range of $3.5 \leq M \leq 6.0$, sourced from the catalog of the Iranian Seismological Center (ISC). A great chunk of the earthquakes in this dataset were relocated by Roostaee et al. (2021) where they used a two-step process to relocate the events. Initially, they estimated a 1D velocity model in the study area, then they used the estimated model to the phases of the earthquakes to relocate them. For the events relocated by Roostaee et al. (2021), we used their location instead of the location of ISC catalogue. Waveforms of events were captured by 22 permanent broadband seismometers (Fig. 2) positioned within the study region, operated by the Iranian Seismological Center of the Institute of Geophysics at the University of Tehran (IGUT), the Iranian National Seismic Network (INSN), and the Earthquake Research Center of Ferdowsi University of Mashhad (EQRC).

Rayleigh wave group velocity dispersion curves were estimated using the single-station method. The estimation of Rayleigh wave group velocity was carried out by extracting the fundamental mode of Rayleigh wave group velocity dispersion curves using the Frequency-Time Analysis (FTAN) method. This approach, originally developed by Levshin et al. (1972, 1992), involves the application of a series of narrowband Gaussian filters to the seismic data. The FTAN analysis was conducted along various ray paths encompassing the study area. To achieve this, an energy-versus-period diagram of the seismogram's surface wave vertical component was initially constructed,

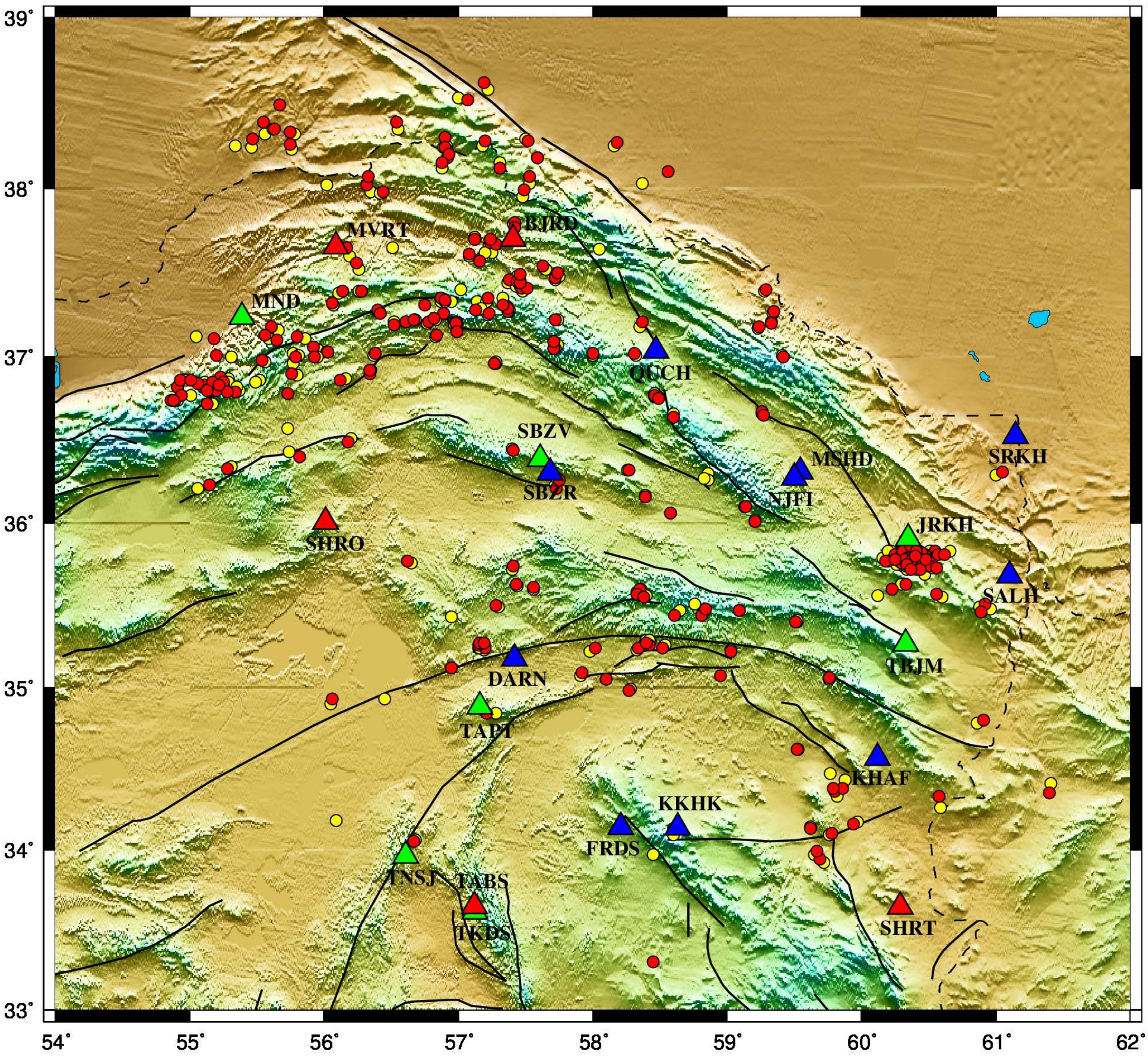

Figure 2. Location map of the broad-band stations and earthquakes used in 2D surface wave tomography. Solid black lines indicate the major active faults. IGUT broad-band stations (green triangles), INSN broad-band stations (red triangles), EQRC broad-band stations (blue triangles), epicenter positions from the catalogue of ISC (yellow circles), relocated epicenters (red circles) from Roostaee et al. (2021).

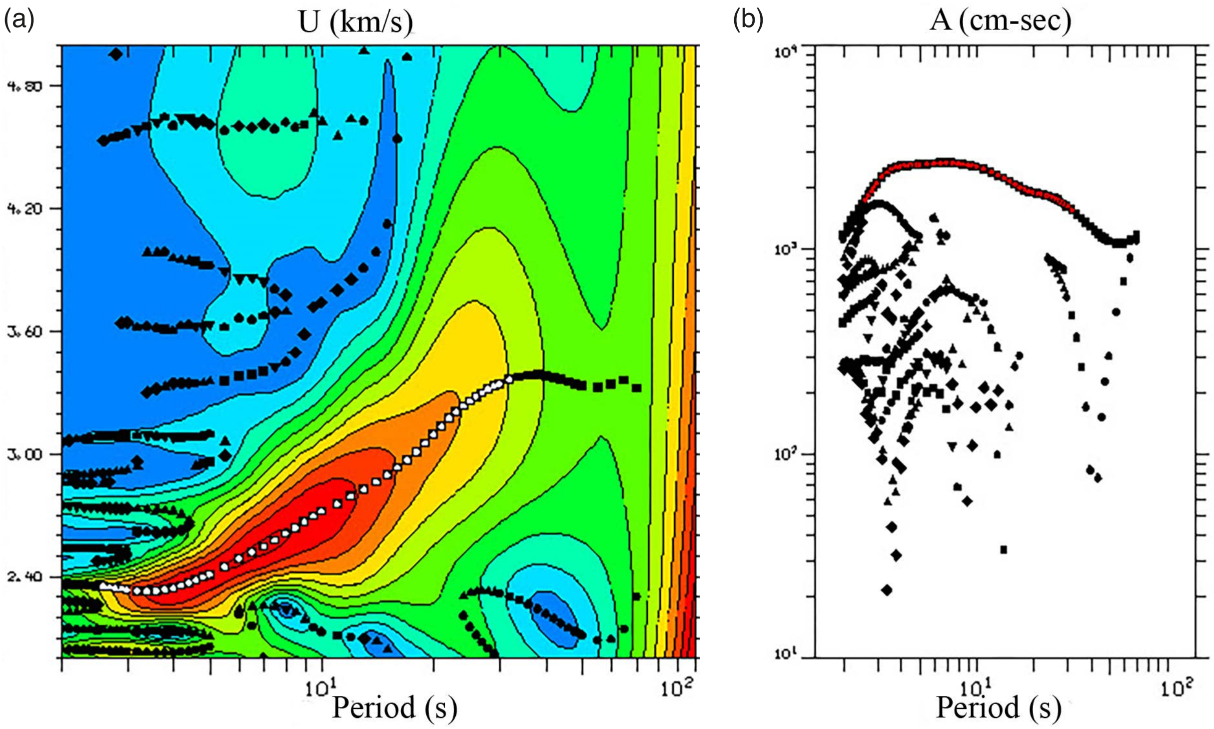

Figure 3. Graphic output of an example of dispersion curve extraction by FTAN. (a) Energy diagram and proposed dispersion curves. The dispersion curves of fundamental and higher modes are shown by suggesting black dotted line while white dotted line is the selected dispersion curve. (b) Spectral amplitudes of corresponding black dotted lines of the left panel. The red dotted line is the spectral amplitude of the selected dispersion curve (white dotted line in (a)).

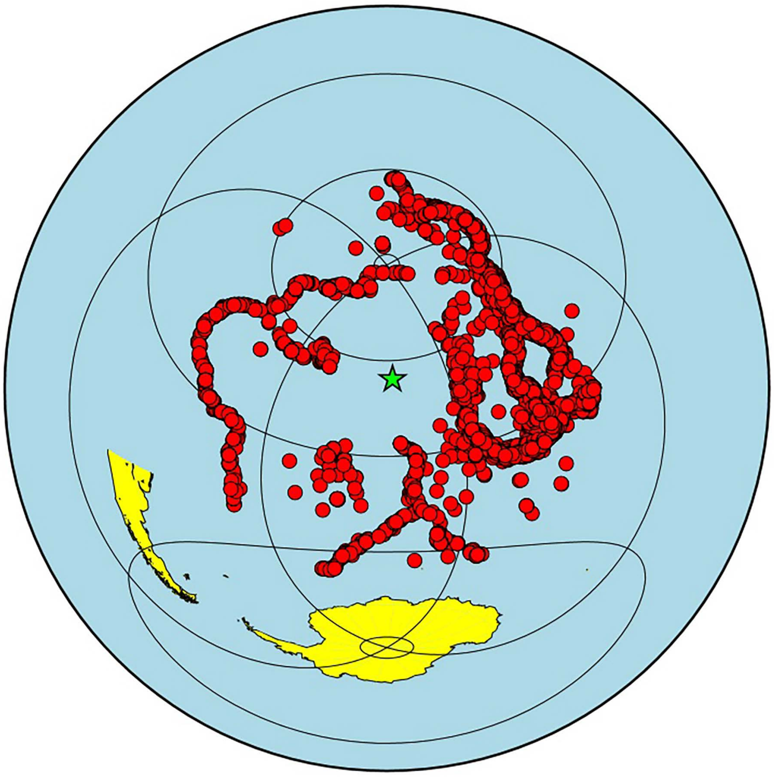

Figure 4. Azimuthal distribution of teleseismic events (red circles with a magnitude range of $5.0 \leq M \leq 7.3$ and epicentral distances of 30 to 95 degrees from the center of our study area (green star).

and the energy maximum corresponding to the Rayleigh-wave fundamental mode was manually identified. Subsequently, the desired fundamental mode surface-wave signal was extracted. An illustrative example of the FTAN analysis conducted on a selected event is presented in Fig. 3, showcasing the extraction of the dispersion curve.

To build our dataset for the receiver function analysis, we used teleseismic earthquakes (Fig. 4) that occurred at epicentral distances ranging from 30° to 95° from the center of our study region, with magnitudes greater than 5 and less than 7.3, and within the time window of 2012-2018. Waveforms of the events in this dataset were recorded by 19 broadband and 4 short-period seismic stations (Fig. 5) located within the study region. Specifically, 4 short-period and 7 broadband stations were operated by IGUT, 4 broadband stations were operated by INSN, and 8 broadband stations were operated by EQRC. The locations of these stations are illustrated in Fig. 5. Table 1 provides detailed information of the stations used for receiver function and surface wave tomography in this study.

To calculate the P receiver functions we did a visual inspection to use only events with good quality and high signal-to-noise ratio. Then, a time window was employed to isolate the segment of the signal necessary for obtaining the receiver function. In this study, a time window of 120 s centered around the P-wave arrival time was applied to all three components of waveforms. Subsequently, processing steps were executed on the raw data to extract the receiver function. These processing steps included removing the mean, trend and instrument responses, filtering

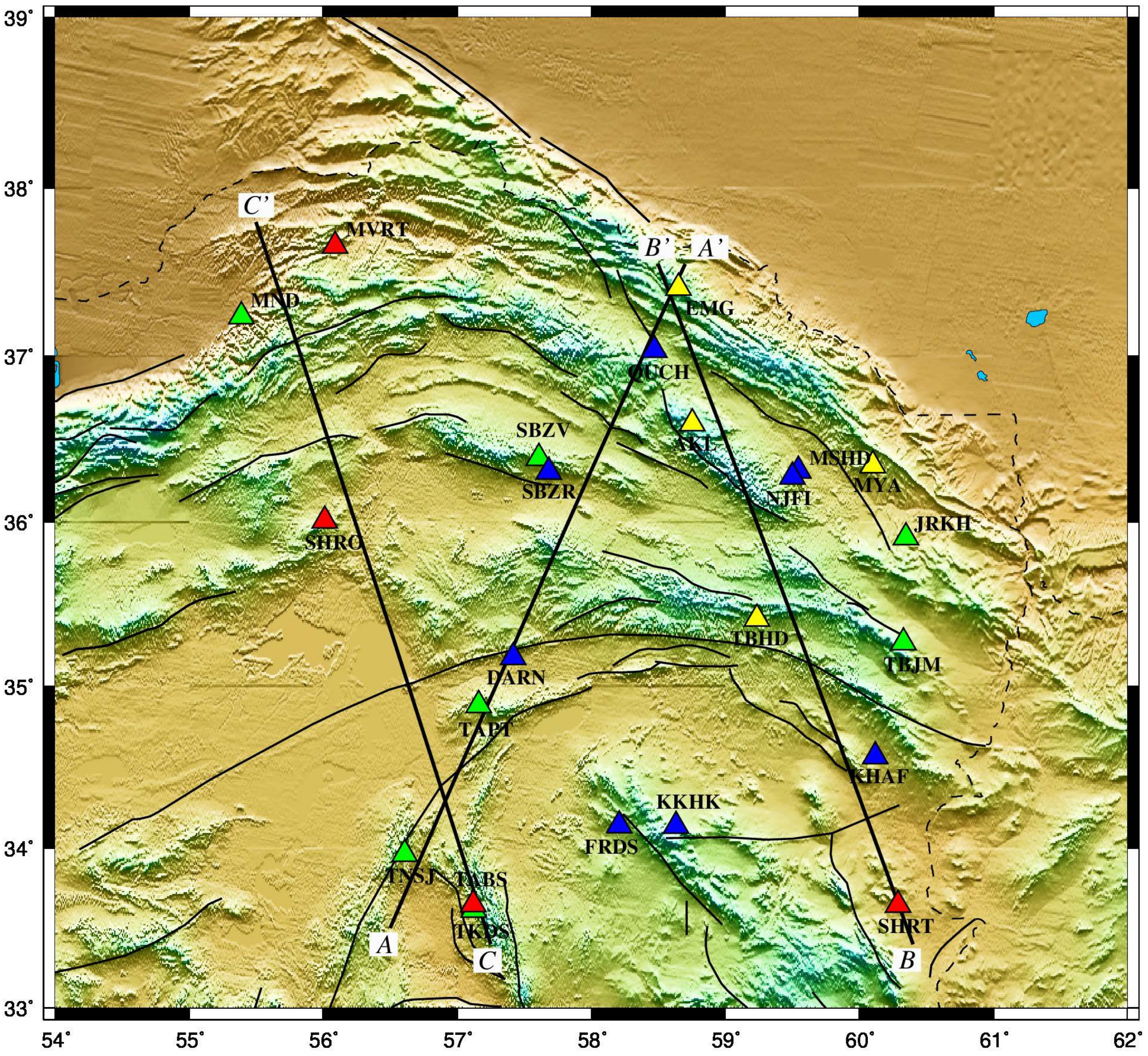

Figure 5. The locations of stations were used to compute P receiver function. Solid black lines indicate the major active faults. IGUT broad-band stations (green triangles), IGUT short-period stations (yellow triangles), INSN broad-band stations (red triangles) and EQRC broad-band stations (blue triangles). The solid black straight lines indicate the sections along which the shear wave velocity variations are obtained.

	Longitude (°), Latitude (°)	Elevation (km)	Instrument type	Network	Station name
Broad-band	56.089°E, 37.659°N	870	CMG-3T	IIEES	**MRVT**
	56.013°E, 36.009°N	1264	CMG-3T	IIEES	**SHRO**
	60.291°E, 33.646°N	837	CMG-3T	IIEES	**SHRT**
	57.119°E, 33.649°N	1106	CMG-3T	IIEES	**TABS**
	57.419°E, 35.176°N	840	CMG-3T	EQRC	**DARN**
	58.210°E, 34.139°N	1490	CMG-3T	EQRC	**FRDS**
	58.634°E, 34.137°N	1680	CMG-3T	EQRC	**KKHK**
	60.122°E, 34.566°N	1010	CMG-3T	EQRC	**KHAF**
	59.535°E, 36.311°N	1024	CMG-3T	EQRC	**MSHD**
	58.470°E, 37.038°N	1504	CMG-3T	EQRC	**QUCH**
	57.683°E, 36.305°N	1281	CMG-3T	EQRC	**SBZR**
	59.500°E, 36.275°N	1188	CMG-3T	EQRC	**NJFI**
	55.389°E, 37.237°N	200	Trillium-120P	IGUT	**MND**
	57.611°E, 36.388°N	2034	Trillium-120P	IGUT	**SBZV**
	60.349°E, 35.908°N	1206	Trillium-120P	IGUT	**JRKH**
	60.329°E, 35.268°N	1741	Trillium-120P	IGUT	**TBJM**
	57.150°E, 34.880°N	1248	Trillium 40	IGUT	**TAPT**
	56.60°E, 33.96°N	1123	Trillium 40	IGUT	**TNSJ**
	57.12°E, 33.61°N	1206	Trillium 40	IGUT	**TKDS**
Short-Period	58.651°E, 37.409°N	2547	SS1	IGUT	**EMG**
	58.754°E, 36.595°N	2510	SS1	IGUT	**AKL**
	60.102°E, 36.344°N	1684	SS1	IGUT	**MYA**
	59.236°E, 35.413°N	1760	SS1	IGUT	**TBHD**

Table 1. Characteristics of all stations used in this study.

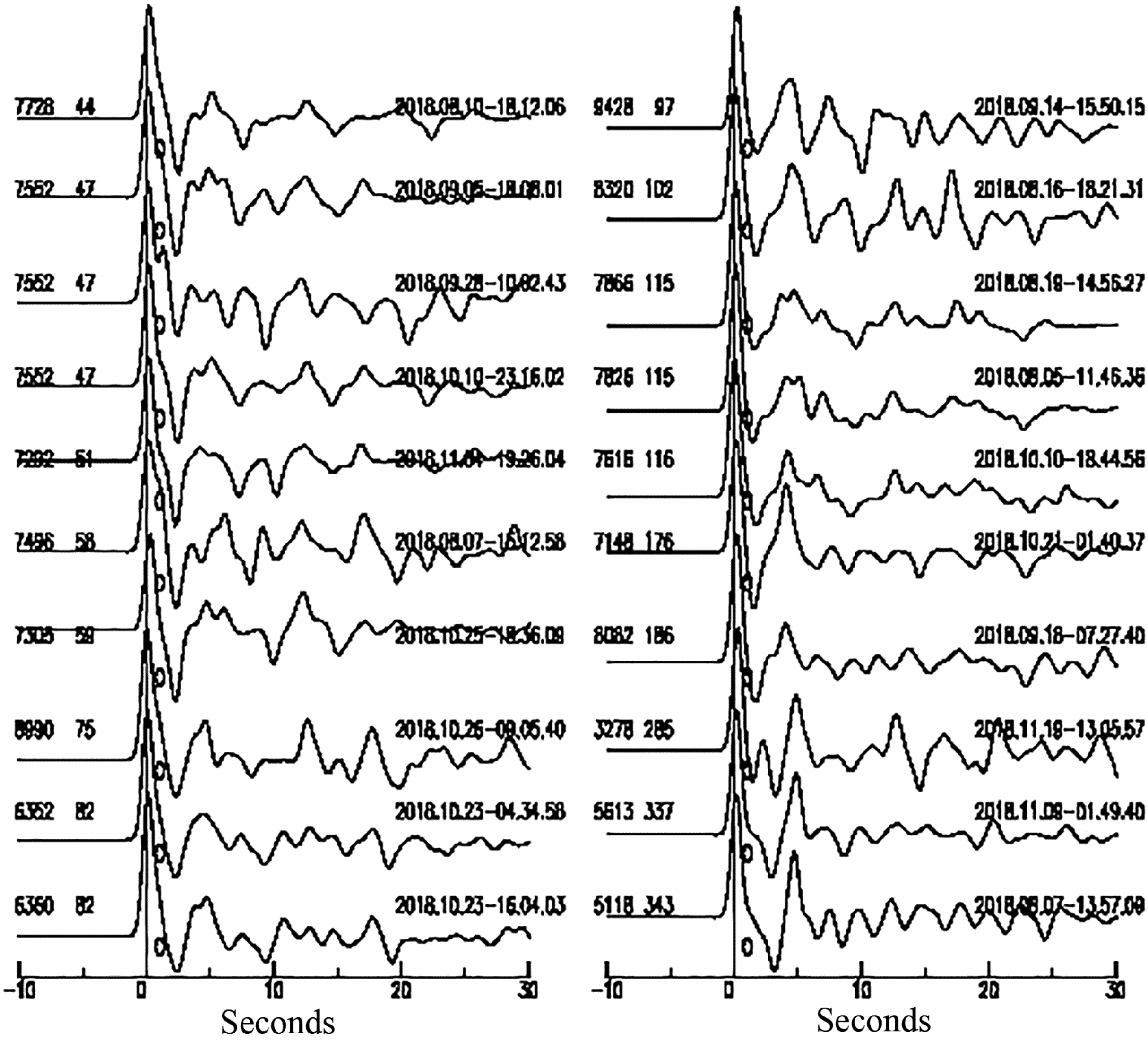

Figure 6. An example subset of the computed receiver functions from station TAPT. The number on the left side of each receiver function represents the distance in km and the back azimuth in degrees from left to right, respectively. The numbers on the right side of each receiver function represent the origin time of the event.

of the waveforms using a gaussian filter with smoothing factor of 1.8 (equivalent to a low-pass filter), rotation of waveforms from ZNE to ZRT using the back-azimuth of the event, applying the iterative time-domain deconvolution process (Ligorria and Ammon, 1999) to obtain the receiver function. Finally, we stacked all the calculated receiver functions of each station after removing the source-station distance effect on receiver functions, utilizing a moveout correction (Kind et al., 1988; Zhu et al., 2000). The stacking process improves the quality of the final stacked receiver function and increases its signal-to-noise ratio. For example, Fig. 6 illustrates an example subset of the individual computed receiver functions from station TAPT used in the stacking process.

5. Results

To obtain local dispersion curves from tomography, we employed the individual dispersion curves of the Rayleigh wave group velocity for each source-station path. Tomography was employed to generate Rayleigh wave group velocity maps for periods of 5, 10, 15, 20, 25, 30, 40, 50, and 60 seconds, with a cell size of 0.5° 0.5°. The number of paths and average distance for each period, in the range of 5 to 60 s, are shown in Table 2.

The process of calculating group velocity maps involved testing several regularization parameters. Decreasing the parameter α resulted in a better fit to the data but generated a solution with increasing artifacts. Conversely,

Period (s)	Number of paths	Average distance (km)
5	555	245
10	974	295
15	981	299
20	874	303
25	734	308
30	575	309
40	230	288
50	112	264
60	48	262

Table 2. Number of paths and average distance for each considered period.

increasing α led to a smoother solution with a poorer fit to the data. Ultimately, we opted to use $\alpha = 0.2$, which provided relatively smooth maps with a minor solution error.

The ray path coverage, averaging area, stretching parameter and estimated errors that are considered as quality controlling parameters for tomography results, obtained for all of the used periods in the tomography procedure. Here, we illustrated these parameters only for a period of 20 s (because of good ray crossing and coverage) as an example of the tomography results in Fig. 7 while for the rest of periods this information is available in the electronic supplementary. Our results show that the distribution of ray paths across different azimuths is notably uniform, indicating satisfactory coverage (see Fig. 7a for a period of 20 s and electronic supplementary for the other periods). The averaging area map provides insights into the dimensions of resolution power of the tomographic procedure within the study area. Smaller averaging areas imply higher resolution power, suggesting a denser network of ray paths, whereas larger averaging areas indicate lower resolution power. Notably, the tomographic results exhibit higher resolution in central regions and within the averaging area of 50 to 150 or 200 km, but resolution power diminishes towards the edges due to weaker path coverage (Fig. 7b for a period of 20 s and electronic supplementary for the other periods). The stretching parameter and estimated errors are the other parameters we used for controlling the quality of tomography results (Fig. 7c and 7d for a period of 20 s, respectively; the electronic supplementary for the other periods). We clipped the maps of these parameters by an averaging area contour line of 200 km, with a solid red line marking the 150 km contour line. This delineation helps to visualize the regions where reliable tomographic data is obtained. Stretching parameter, indicates that in most parts of central areas we have a nearly uniform azimuthal distribution with almost no preferred orientation of ray paths ($E \leq 0.5$). The distribution of estimated errors within the clipped area is less than 0.05 km/s, implying the high accuracy of the tomography results in the clipped area.

We mapped the Rayleigh wave group velocities as the final results of the 2D surface wave tomography for all the selected periods (Fig. 8 for a period of 20 s and electronic supplementary for the other periods). These maps provide valuable insights into the distribution of dispersion characteristics of Rayleigh wave group velocities within the study area.

As, the group velocity distribution within the region has been computed at nodes of a $0.5° \times 0.5°$ grid; the dispersion curve and its relevant errors for each station used in receiver function can be derived by averaging the velocities at four corner of the $0.5° \times 0.5°$ cell containing that station. To compute the 1D velocity structure beneath each station, the receiver functions acquired for each station along with the group velocity dispersion

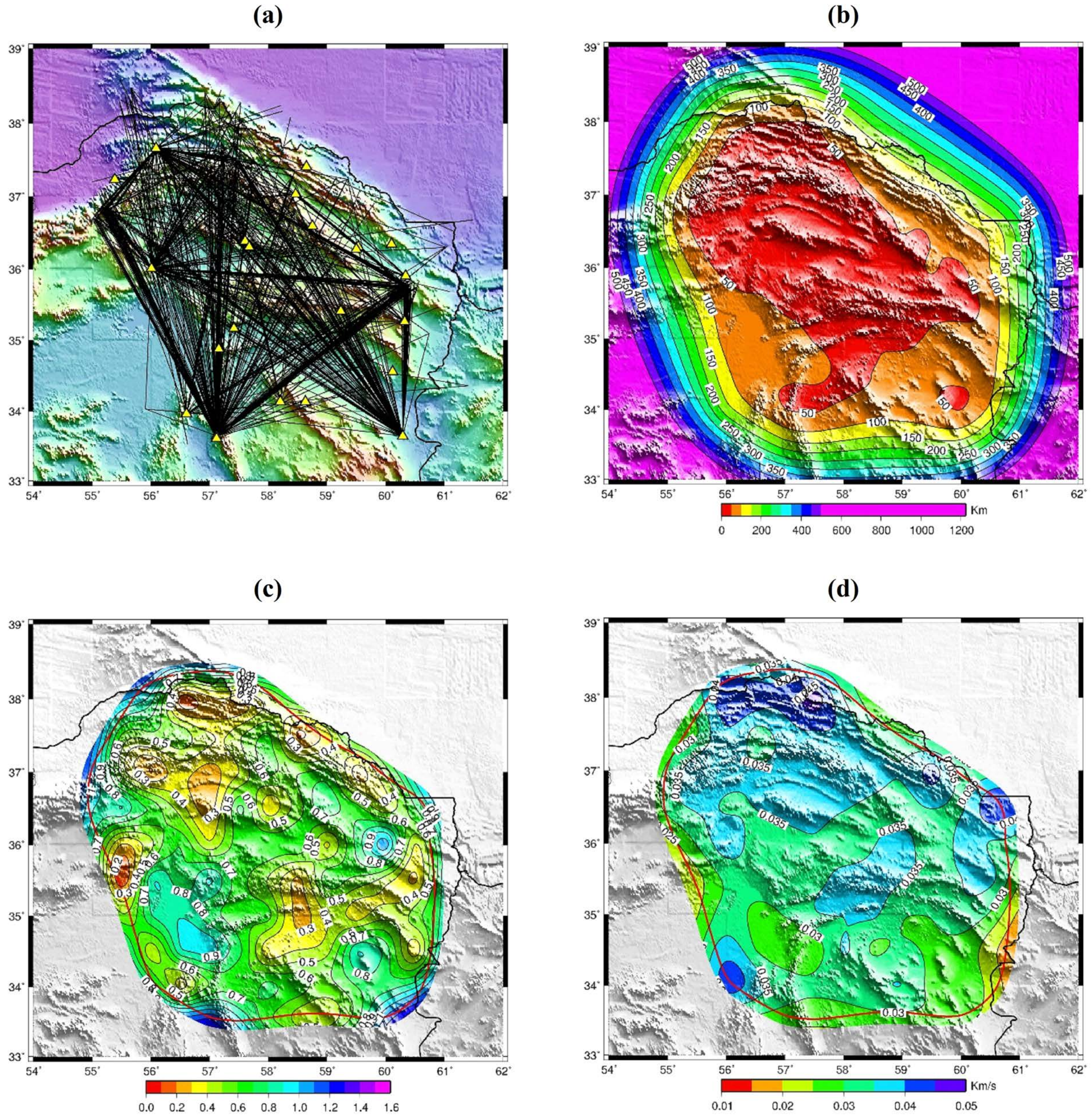

Figure 7. Distribution of parameters for controlling the quality of tomographic maps for a period of 20 s. (a) Ray path distribution; (b) averaging area; (c) stretching parameter; (d) estimated errors. In (c) and (d), the images are clipped by averaging the area contour line of 200 km while the 150 km contour line is plotted by solid red line.

curves obtained from the 2D tomography, are employed as input parameters for a simultaneous inversion process. This approach yields a comprehensive and accurate 1D shear wave velocity model beneath each station.

We performed joint inversions across a range of values of the P parameter to optimize the agreement between observed and predicted receiver functions and surface wave dispersion curves. Finally, we selected the value $P = 0.3$ which resulted in the simplest model that best fit both the dispersion curve and receiver function datasets by visual inspection. We selected a half-space model with a constant shear wave velocity as our initial model for inversion procedure. From Earth surface to the depth, this model has a number of 30 layers with 2 km thickness down to depth of 60 km, followed by a number of 8 layers with 5 km thickness down to the depth of 100 km and a number of 5 layers with 10 km thickness down to the depth of 150 km, where the initial value of shear wave velocity of all the layers is 4.28 km/s. For the rest of the model, we used the IASP91 global velocity model.

After obtaining the shear wave velocity model by joint inversion procedure, we simplified and refined the resulting shear wave velocity model. This involved simplifying the model to feature a smaller number of layers.

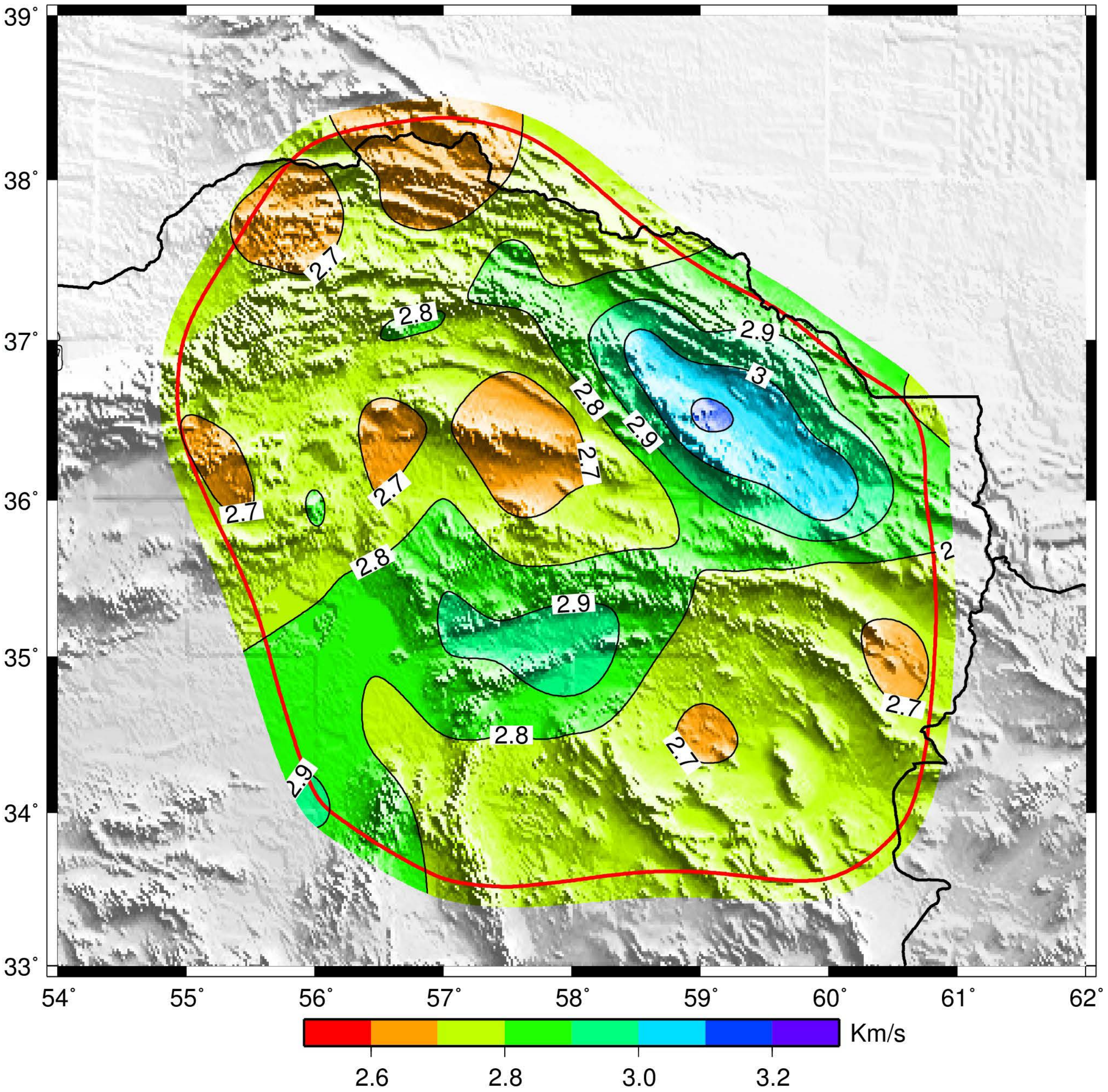

Figure 8. Tomographic map of Rayleigh wave group velocities for a period of 20 s. The image is clipped by averaging the area contour line of 200 km while the contour line of 150 km is plotted by a solid red line

To achieve this, we first identified the primary velocity boundaries within the model. After that, we eliminated distortions and minute structures from the model. Subsequently, we calculated the average velocity of the layers situated between the assumed boundaries. Utilizing forward modeling, we simulated synthetic receiver functions and dispersion curves for the final simplified model. Our model selection criterion was that the synthetic curves and receiver function should align with the experimental error bars and have the best fit between synthetic and observed data. The outcomes of simplifying the inverted velocity model for the 23 stations employed in our study are presented in Fig. 9. This approach enhances the interpretability and reliability of the velocity model, making it more consistent with observed data while still accounting for the inherent uncertainties in the measurements. The Moho depth values for all the stations from the simplified model are provided in Table 3.

By incorporating 1D velocity models beneath each station and employing interpolation for other points, we are enabled to visualize the 2D velocity structure across hypothetical profiles that traverse these stations. Our approach involves considering three profiles oriented in distinct directions, intersecting significant geological and tectonic features of the region. These profiles serve to investigate the intricate structures within the area. The geographical placement of these profiles is depicted in Fig. 5.

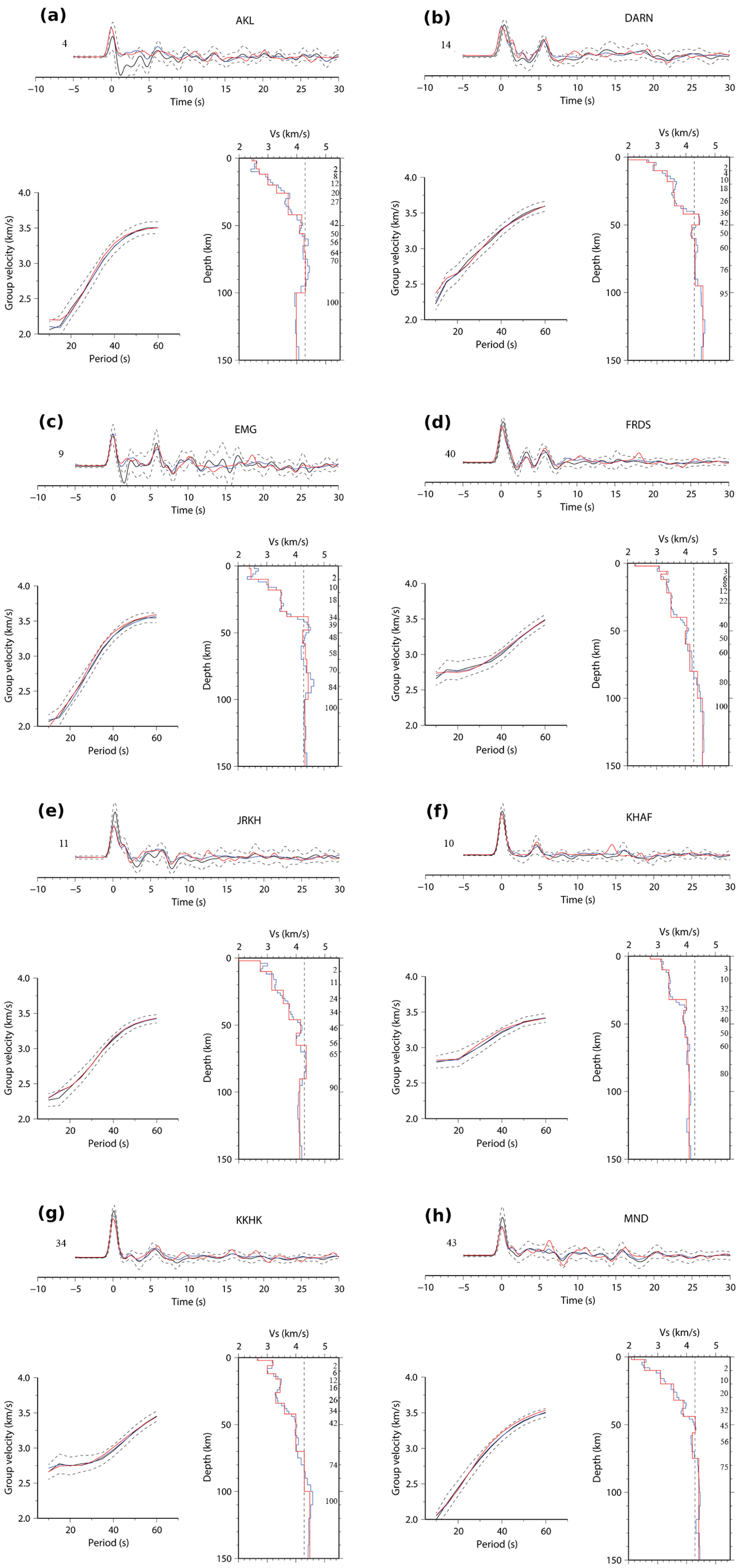
(a)
AKL
4
(b)
DARN
14
(c)
EMG
9
(d)
FRDS
40
(e)
JRKH
11
(f)
KHAF
10
(g)
KKHK
34
(h)
MND
43
Time (s)
Group velocity (km/s)
Period (s)
Vs (km/s)
Depth (km)

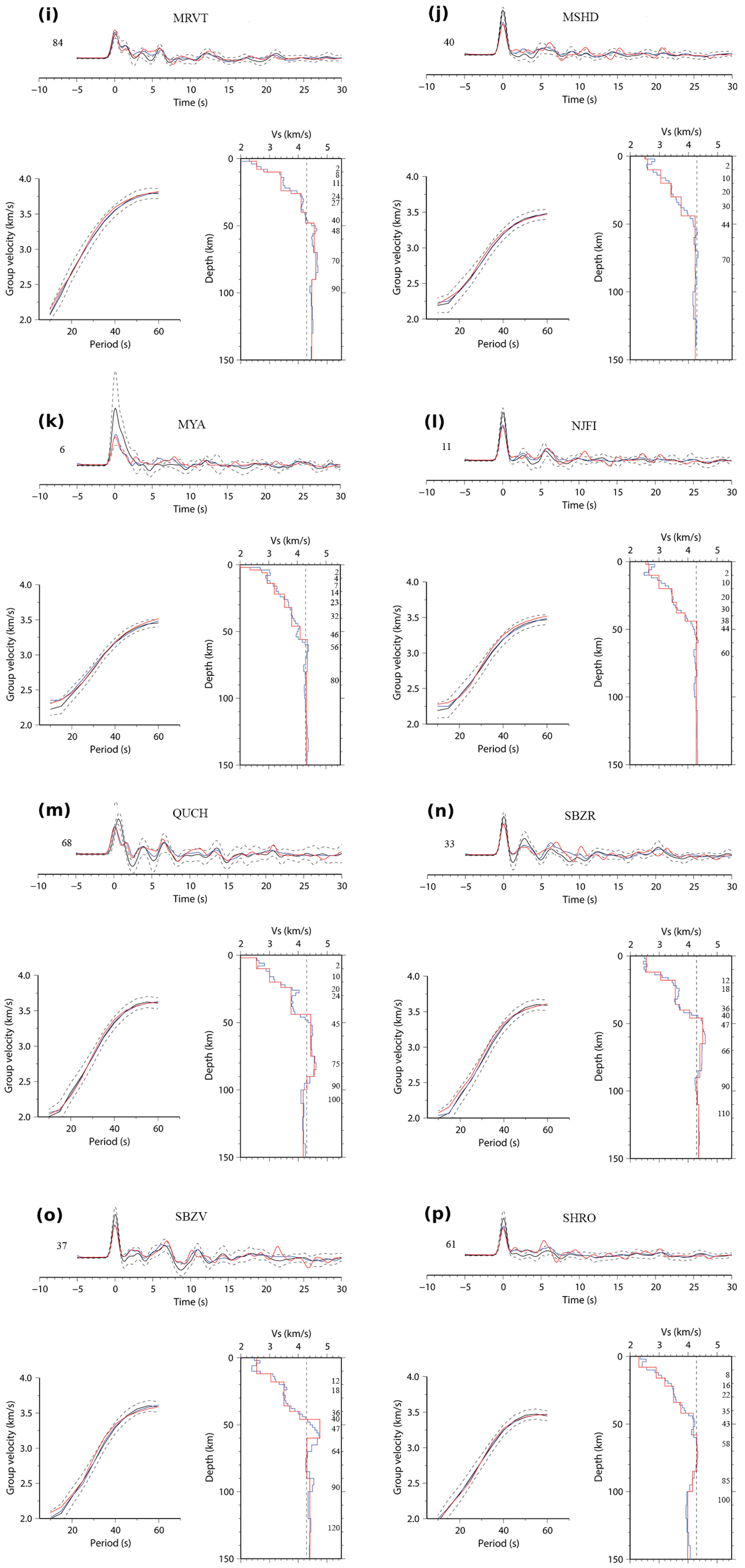
(i)
MRVT
84
(j)
MSHD
40
(k)
MYA
6
(l)
NJFI
11
(m)
QUCH
68
(n)
SBZR
33
(o)
SBZV
37
(p)
SHRO
61
−10
−5
0
5
10
15
20
25
30
Time (s)
Group velocity (km/s)
2.0
2.5
3.0
3.5
4.0
20
40
60
Period (s)
Vs (km/s)
2
3
4
5
Depth (km)
0
50
100
150

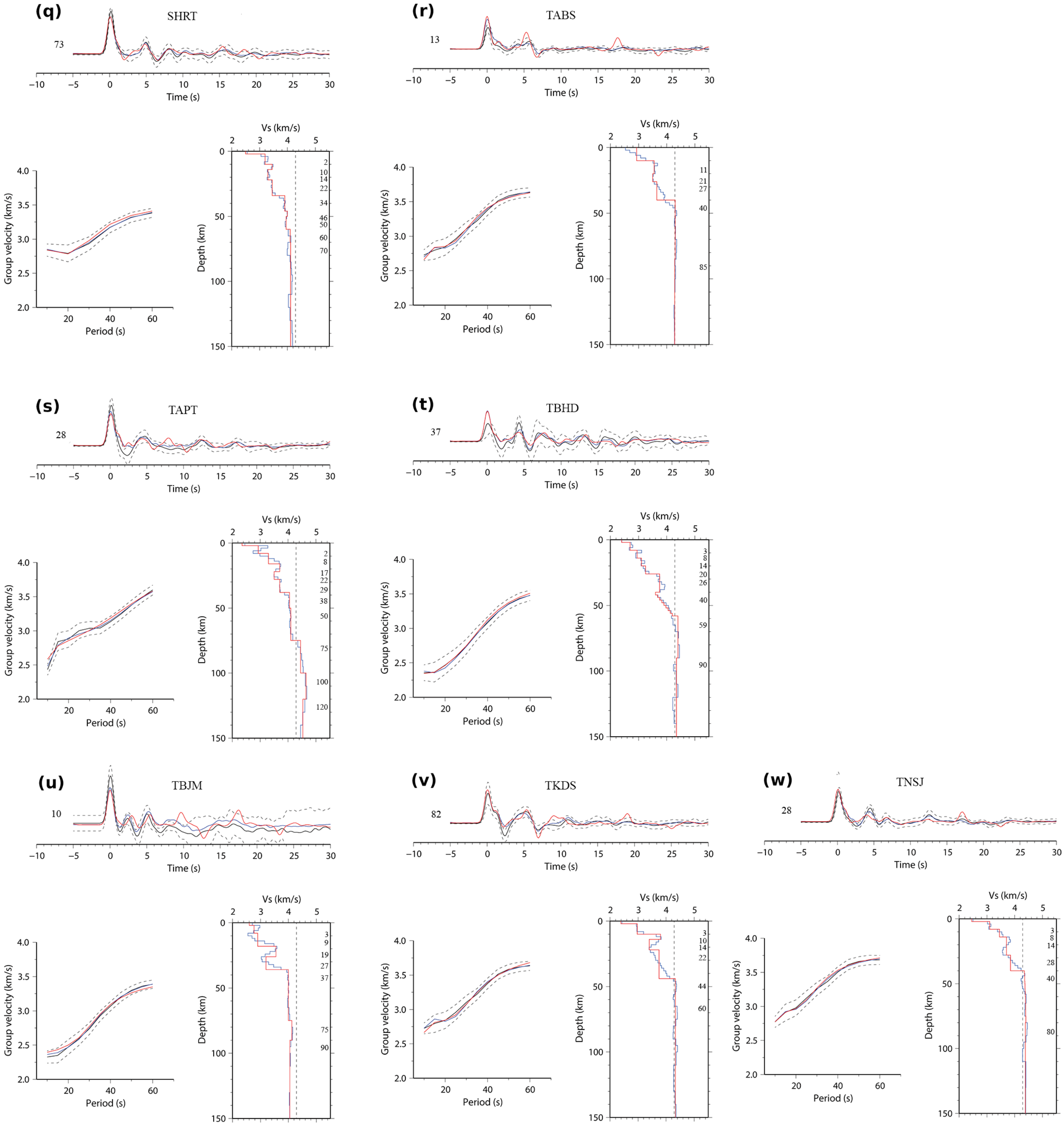

Figure 9. Simplification of the inverted model for 23 stations (Panels (a) to (w)). In Each panel; (Top) The observed stacked receiver function is represented by the black line, with error bars indicated by the dashed black line. The synthetic receiver function derived from the velocity model obtained through joint inversion is shown in blue, while the synthetic receiver function calculated from the simplified crustal model is depicted in red. The arrival time of the direct P wave is marked as t = 0. The number on the left corresponds to the number of stacked receiver functions. The name of the station is written on top of the plotted receiver function. (Bottom left) The observed group velocity is represented by the solid black line, with error bars indicated by the dashed black lines. The synthetic group velocity derived from the velocity model obtained through joint inversion is shown in blue, while the synthetic group velocity calculated for the simplified crustal model is depicted by the solid red line. (Bottom right) The velocity model obtained from joint inversion is illustrated by the solid blue line, the initial velocity model is represented by the dashed black line, and the simplified crustal model, considered as the final model, is shown by the solid red line.

Station name	Moho depth (km)	Station name	Moho depth (km)	Station name	Moho depth (km)
MRVT	48	MSHD	44	TNSJ	40
SHRO	43	QUCH	45	TKDS	44
SHRT	34	SBZR	47	EMG	39
TABS	40	NJFI	44	AKL	42
DARN	42	MND	45	MYA	56
FRDS	40	SBZV	47	TBHD	50
KKHK	42	JRKH	46	TAPT	38
KHAF	32	TBJM	37		

Table 3. Moho depth obtained from forward modeling for each station.

Figures 10, 11, and 12 present the 2D shear wave velocity sections along profiles AA′, BB′, and CC′, respectively. For each profile, after selecting the stations close to the profile (by visual inspection) we projected them along the profile to find the stations location; then for each station we attributed the velocity of each layer to its middle depth; finally, we mapped the 3 columns data of station position along the line, depth and shear wave velocity for each line to produce the cross-section maps.

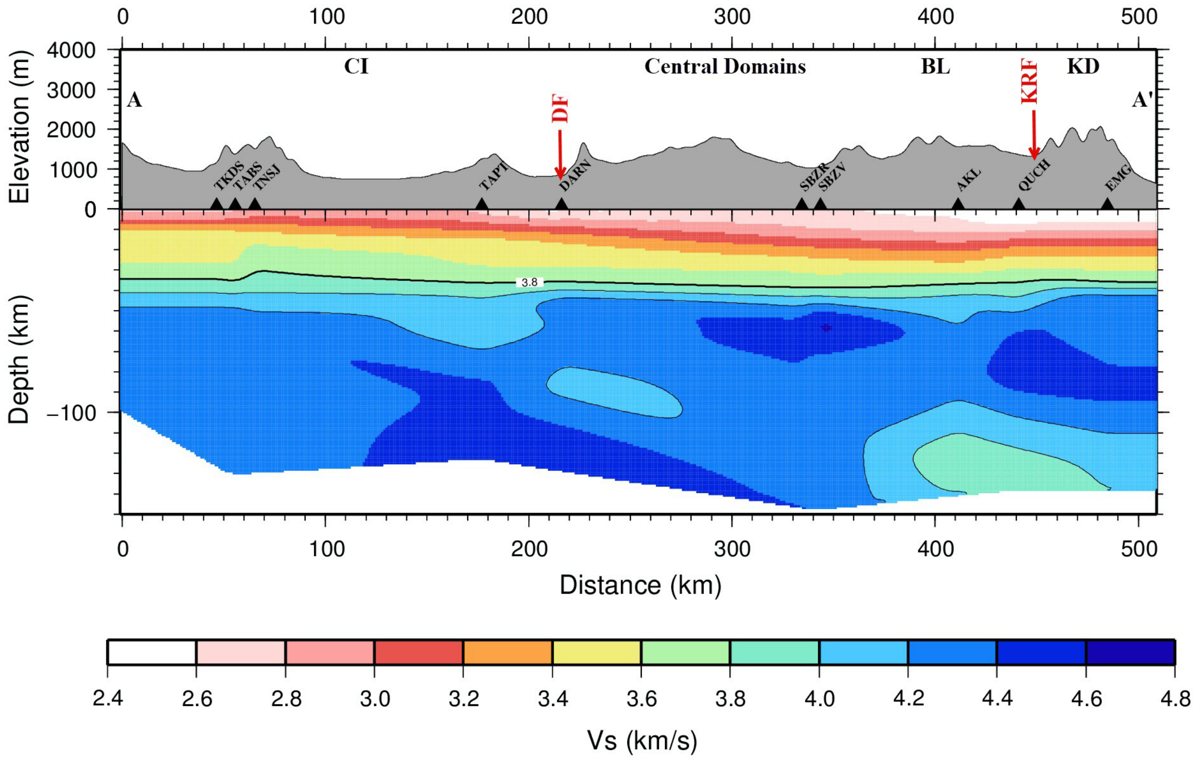

Figure 10. (Bottom) Distribution of shear wave velocity (V_S) along profile AA′. (Top) Topography profile, with main tectonic units, and major faults (red arrows). Triangles represent the projection of the used stations for making this cross section.

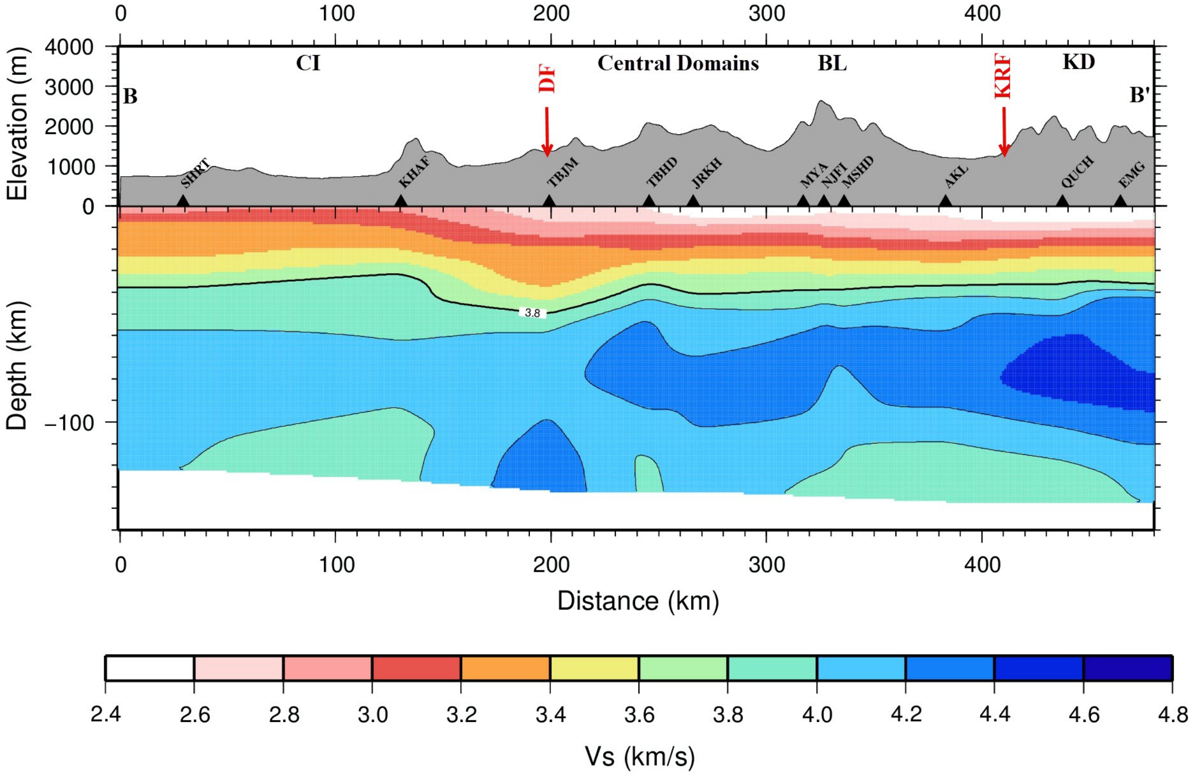

Figure 11. (Bottom) Distribution of shear wave velocity (V_S) along profile BB′. (Top) Topography profile, with main tectonic units, and major faults (red arrows). Triangles represent the projection of the used stations for making this cross section.

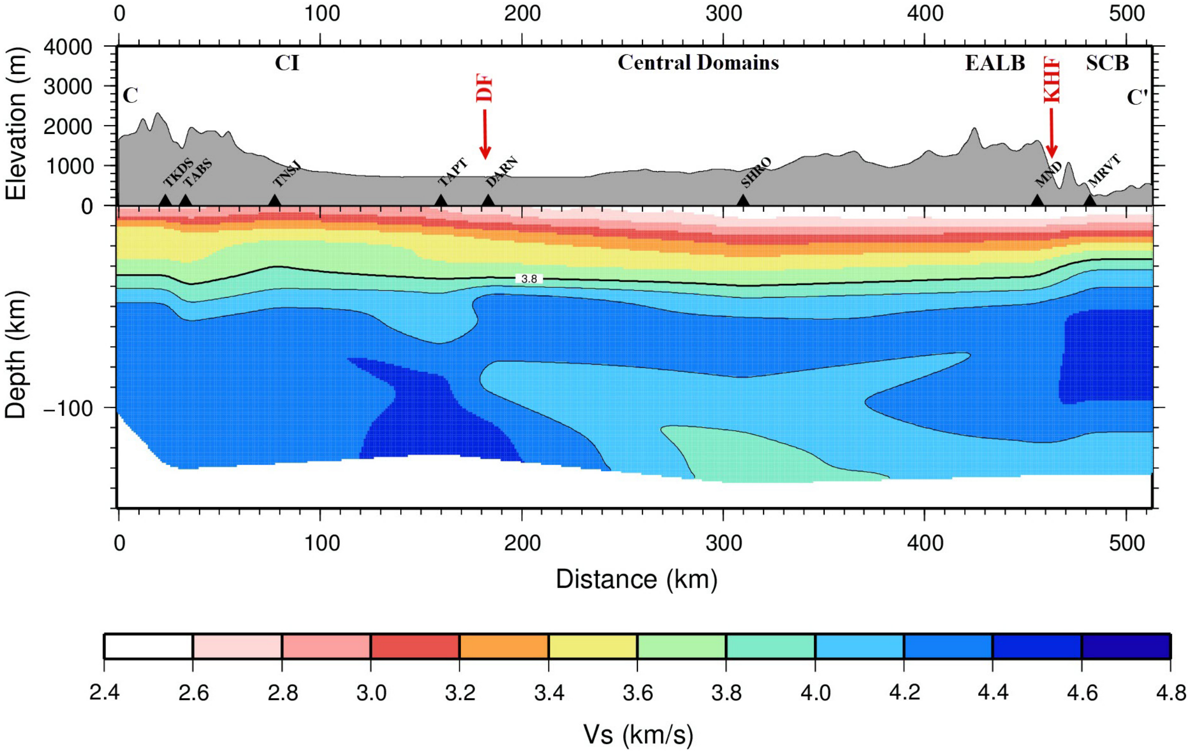

Figure 12. (Bottom) Distribution of shear wave velocity (V_S) along profile CC′. (Top) Topographic profile, with main tectonic units, and major faults (red arrows). Triangles represent the projection of the used stations for making this cross section.

In profile AA′, a distinct pattern emerges where the low-velocity layers within the upper crust exhibit contrasting characteristics. The northeastern segment of the profile, encompassing areas under KD and BL, displays notably thicker low-velocity layers compared to the southwestern counterpart, covering CI. This variation can be attributed to the thickened sedimentary, mountainous terrain and folded sedimentary in the latter regions, resulting in an increased thickness of low velocity layers. The velocity structures in CI are simpler with fewer tectonic alterations, thus leading to a reduction in the thickness of low-velocity upper crust layers. In the context of profile BB′, akin to profile AA′, the thickness of the low-velocity layers is notably higher on the right section, corresponding to the northern domains of DF, covering the areas beneath KD and BL mountains. In contrast, the left side of the section, encompassing the CI, demonstrates thinner low-velocity layers.

It becomes evident, particularly in the vicinity of the DARN station located within DF range, that a significant lithospheric-scale tectonic boundary is present. This boundary is observable both in the crust and upper mantle through distinct changes in the velocity structure. This observation aligns with the understanding that DF, situated at the northern edge of CI, delineates the border with BL and KD mountains. In summary, profiles AA′ and BB′, the disparity on either side of DF is discernible. This is analogous to the variation in low-velocity layers on the northern and southern flanks of the fault (right and left sections), a distinction arising from structural dissimilarities between the CI and the KD and BL regions.

Profile CC′, which encompasses the MND and MRVT stations, offers insights into the SCB presence and its interaction with the Iranian microplate. The distinctive characteristic of the SCB lies in the oceanic-like layer with velocities ranging between 3.9-4.1 km/s within the crust. This layer becomes evident at MRVT station within the depth range of 27-48 km and below MND station within the depth range of 32-45 km. The higher-velocity layer corresponds to the basalt layer of the oceanic-like plate in the SCB. This layer’s contour line at 4 km/s undergoes an upward shift beneath these stations, revealing an elevated high-speed layer within the upper crust. Furthermore, a distinct variation in lithospheric structure becomes apparent within this region, indicating that the crust and upper mantle under these stations differ from the rest of the section, all due to the presence of the SCB.

6. Discussion

We have successfully established the crustal and upper mantle velocity structure beneath 23 seismic stations situated in NE Iran. This area encompasses the KD and BL mountain ranges, the northern parts of CI, and some regions of the SCB. Our approach involved the joint inversion of receiver functions and the dispersion curves of Rayleigh wave group velocities. A comprehensive summary and comparison of our findings for NE Iran with those presented in previous geological and geophysical investigations is as follows.

Our results distinctly highlight prominent changes in velocity structure along both the northern and southern flanks of the DF, occurring at both the crustal and lithospheric scales (Figs. 10-12). This fault boundary can consequently be characterized as a microplate demarcation. Our observations are consistent with earlier studies conducted by Wellman (1965), Stocklin et al. (1973), Javadi et al. (2013), and Tadayon et al. (2019), all of which have similarly designated this fault as the northern limit of the CI.

Our study reveals significant variations in the average thickness of low-velocity layers within the upper crust and sedimentary cover, particularly between the CI and the KD and BL mountain ranges (Figs. 10 and 11). The upper crust and sedimentary layers with an average shear wave velocity of approximately 3.0 km/s are around 10 km thick on the southern flank of the DF and approximately 20 km beneath the KD and BL ranges. The increased thickness of low-velocity layers beneath the KD and BL ranges is associated with ongoing shortening processes resulting from the convergence of the Iran and Turan plates, the presence of thickened sedimentary layers, mountainous terrain, and folded sedimentary structures in these regions.

Between the KD and BL mountains, an intriguing crustal behavior unfolds (Figs. 10 and 11). Here, the crust thickens, and the presence of distinct high-velocity layers on either side of the KRF, coupled with a high-velocity layer curving from the northeastern to southwestern aspects, particularly beneath BL, signifies the role of the KRF as a collision boundary between the Turan platform and the Iranian microplate. Therefore, this structural curvature can be linked to the closure of the Palaeotethys Ocean.

Our study reveals a simpler velocity structure and thinner low-velocity layers within the upper crust across the southern flank of DF, coinciding with the CI region (Figs. 10 and 11). Stations situated in this region exhibit less deformation related to those positioned over the BL and KD ranges, due to its less tectonically active nature. Our findings are in concordance with those presented by Motaghi et al. (2012) through receiver function analysis and Motaghi et al. (2014) obtained by the simultaneous inversion of data from receiver function and fundamental mode Rayleigh wave group velocity for the Iranian plateau, validated by the modeling of Bouguer gravity anomaly data. This consistency across various studies validates and reinforces our understanding of the complex geological and tectonic dynamics underlying the NE Iran.

As mentioned before DF is divided into three distinct segments with different fault systems (Javadi et al., 2013; Farbod et al., 2011). Within the scope of our study, we conducted profiles AA′ and CC′, which traverse the central or western segment of the DF, while profile BB′ traverses the eastern portion of the DF. Examining the shear wave velocity sections along profile BB′ reveals a distinctive northward dip in the eastern segment of DF (Note the northward dipping of crustal layers beneath DF mark in Profile BB′; Fig. 10). This observation aligns with the geological characteristics previously identified in the region, contributing to our understanding of the fault system's dynamics and structure (Javadi et al., 2013; Farbod et al., 2011)

The average Moho depth in the studied region is estimated to be approximately 40 km. The thickest crust, measuring around 56 km beneath the MYA station, is situated between the BL and KD mountain ranges along and very close to the KRF, which is recognized as the suture zone resulting from the collision between Iranian plateau and Eurasia. The thinnest crust depths were observed at the KHAF station (32 km) and the SHRT station (34 km), both located on the southern flank of the eastern part of DF. Notably, no abrupt changes in Moho depth were identified along the western and central parts of DF.

The northwestern expanse of our study area is bounded by the SCB. Our study outcomes unveil a distinct crust and lithospheric structure within this basin, setting it apart from the adjoining regions. Scrutinizing the lateral shifts in shear wave velocity across the middle crust, lower crust, and upper mantle, a discernible contrast in the velocity structure emerges between NE Iran beneath the KD and BL ranges and the SCB. In profile CC′ (Fig. 12), beneath the MRVT and MND stations, the crust reveals a three-layered structure (Figs. 9 and 12). The uppermost layer exhibits low velocity and is likely composed of significant sediment deposits. The second layer, extending to approximately 30 km in depth, appears to consist of granite with a distinct velocity structure differing from its surroundings. Below this lies the high velocity (~4 km/s) lower crust, about 20 km thick, characterized by a pronounced disparity in shear wave velocity compared to the middle crust and adjacent areas, that are compatible with the presence of oceanic crust, hinting at an oceanic-like nature within the SCB crust. Additionally, the velocity of the upper mantle beneath MRVT and MND stations exceeds that of neighboring regions. This velocity variation extends through the crust and lithosphere, suggesting that the lithosphere of the SCB is inherently more rigid and has higher velocities than adjacent areas. These findings are consistent with previous studies by Mangino et al. (1998), reinforcing our understanding of the unique geological and geophysical characteristics defining the SCB and its juxtaposition with surrounding geological formations.

7. Conclusion

In this study, we investigate the crustal velocity structure and Moho discontinuity depth beneath the NE Iran continental collision zone through the joint inversion of P receiver functions and Rayleigh wave group velocity dispersion curves. The results obtained in this study can be summarized as follows:

a) Our results distinctly highlight prominent changes in velocity structure along both the northern and southern flanks of the Daruneh fault, occurring at both the crustal and lithospheric scales. This fault boundary can consequently be characterized as a microplate demarcation.

b) In addition, our analysis indicates that variations in the average thickness of low-velocity layers within the upper crust and sedimentary cover are distinguishable between central Iran and the Kopeh Dagh and Binalud Ranges. The greater thickness of low-velocity layers beneath the Kopeh Dagh and Binalud Ranges correlates with ongoing shortening processes caused by the convergence of the Iran and Turan plates, the presence of thickened sedimentary layers, mountainous terrain, and folded sedimentary structures in these areas.

c) The northwestern expanse of our study area is encompassed by the South Caspian Basin. Our study outcomes unveil a distinct crust and lithosphere within this basin, setting it apart from the adjoining regions. The lateral velocity distribution at the middle crust, lower crust, and upper mantle highlights the differences between NE Iran (specifically the Kopeh Dagh and Binaloud Ranges) and the South Caspian Basin.

Acknowledgments. We thank the Iranian seismological center of Institute of Geophysics of University of Tehran (IGUT), International Institute of Earthquake and Engineering and Seismology (IIEES), and Earthquake Research Center of Ferdowsi University of Mashhad (EQRC) for providing the digital data sets.

References

Alavi, M. (2009). Thrust tectonics of the Binalood Region, NE Iran, Tectonics, 11, 2, 360-370, doi:10.1029/91TC02217.

Aghanabati, A. (2004). Geology of Iran, Tehran: Geological Survey of Iran, 586 (in Persian).

Al-Lazki, A. I., D. Seber, E. Sandvol, N. Turkelli et al. (2003). Tomographic Pn velocity and anisotropy structure beneath the Anatolian plateau (eastern Turkey) and the .surrounding regions, Geophys. Res. Lett., 30, 24, doi:10.1029/2003GL017391.

Al-Lazki, A. I., E. Sandvol, D. Seber, M. Barazangi et al. (2004). Pn tomographic imaging of mantle lid velocity and anisotropy at the junction of the Arabian, Eurasian and African plates, Geophys. J. Int., 158, 1024-1040.

Al-Lazki, A. I., K. S. Al-Damegh, S. Y. El-Hadidy, A. Ghods et al. (2014). Pn velocity structure beneath Arabia-Eurasia Zagros collision and Makran subduction zones, Geol. Soc. Lond. Spec. Publ., 392, 1, 45-60.

Ammon, C. J. (1991). The isolation of receiver effects from teleseismic P waveforms, Bull. Seism. Soc. Am., 81, 2504-2510.

Ammon, C. J., G. E. Randall and G. Zandt (1990). On the non-uniqueness of receiver function inversions, J. Geophys. Res., 95, 15303-15318.

Berberian, M. (1981). Active faulting and tectonics of Iran: Zagros-Hindukush-Himalaya Geodynamic evolution, In Gupta, H. K. and F. M. Delany (eds), Am. Geophys. Union and Geol. Soc. Am., Geodyn., 3, 33-69.

Brunet, M. F., M. V., Korotaev, A. V. Ershov, and A. M. Nikishin (2003). The South Caspian Basin: a review of its evolution from subsidence modelling, Sedimentary Geol., 156, 119-148.

Davoudzadeh, M. and K. Schmidt (1984). A review of the Mesozoic paleogeography and paleotectonic evolution of Iran, Neues Jahrb. Geol., Palaeontol. Abh., 168, 182-207.

Ditmar, P. G. and T. B. Yanovskya (1987). Generalization of Backus-Gilbert Method for Estimation of Lateral Variations of Surface Wave Velocities, Phys. Solid Earth, Izvestia Acad. Sci. USSR, 23, 6, 470-477.

Farbod, Y., O. Bellier, E. Shabanian and M. R. Abbassi (2011). Geomorphic and structural variations along the Doruneh fault system (central Iran), Tectonics, 30, TC6014, doi:10.1029/2011TC002889.

Hollingsworth, J., J. Jackson, R. Walker and H. Nazari (2009). Extrusion tectonics and subduction in the eastern South Caspian region since 10 Ma: REPLY, Geology, 37, 12, e199-e200.

Herrmann, R. B. (2013). Computer programs in seismology: An evolving tool for instruction and research, Seism. Res. Letter., 84, 1081-1088, doi:10.1785/0220110096.

Herrmann, R. B. and C. J. Ammon (2007). Computer Programs in Seismology, version 3,30, Surface Waves, Receiver function and crustal structure, Department of Earth and atmospheric sciences, Sant Louis University, St Louis.

Hessami, K., F. Jamali and H. Tabassi (2003). Major active faults of Iran. International Institute of Earthquake Engineering and Seismology, Tehran.

Jackson, J. and D. McKenzie (1984). Active Tectonics of the Alpine-Himalayan Belt between Western Turkey and Pakistan, Geophys. J. Int., 77, 185-264, doi:10.1111/j.1365-246X.1984.tb01931.x.

Javadi, H. R., M. R. Ghassemi, M. Shahpasandzadeh, B. Guest et al. (2013). History of faulting on the Doruneh Fault System: Implications for the kinematic changes of the Central Iranian Microplate, Geol. Mag., 150, 04, 651-672.

Julia, J., C. J. Ammon, R. B. Herrmann and A. M. Correig (2000). Joint inversion of receiver function and surface wave dispersion observations, Geophys. J. Int., 143, 1, 99-112.

Kind, R., G. L. Kosarev and N. V. Petersen (1995). Receiver functions at the stations of the German Regional Seismic Network (GRSN), Geophys. J. Int., 121, 191-202.

Kind, R. and L. P. Vinnik (1988). The upper mantle discontinuities underneath the GRF array from P-to-S converted phases, J. Geophys. Res., 62,138-147.

Knapp, J. H. and J. A. Connor (2004). Crustal-scale structure of the South Caspian Basin revealed by deep seismic reflection profiling, Mar. Pet. Geol., 21, 1073-1081.

Kosarev, G., K. R. Kind, S. V. Sobolev, X. Yuan et al. (1999). Seismic evidence for a detached Indian lithosphere mantle beneath Tibet: Science., 283, 1306-1309.

Langston, C. A. (1979). Structure under Mount Rainier, Washington, inferred from the teleseismic body waves, J. Geophys. Res., 84, 4749-4762.

Levshin, A. L., V. F. Pisarenko and G. A. Pogrebinsky (1972). On a Frequency-time Analysis of Oscillations, Ann. Geophys, 28, 211-218.

Levshin, A. L., L. Ratnikova and J. Berger (1992). Peculiarities of surface wave peopgation across Central Eurasia, Bull. Seism. Soc. Am., 82, 2464-2493.

Ligorria, J. P. and C. J. Ammon (1999). Iterative deconvolution and receiver-function estimation, Bull. Seismol. Soc. Am., 89, 5, 1395-1400.

Maksimov, S. P. (Ed.) (1992). Kazakhstan and Middle Asia, Book 3, Platform Mantle of the Epi-Paleozoic Plates and Depressions of Middle Asia and South Kazakhstan [in Russian], 6, 148, Nedra, Moscow.

Mangino, S. and K. Priestley (1998). The crustal structure of the southern Caspian region, Geophys. J. Int. 133, 630-648.

Mangino, S. G., G. Zandt and C. J. Ammon (1993). The receiver structure beneath Mina, Nevada, Bull. Seismol. Soc. Am., 83, 2, 542-560.

Masson, F., M. Anvari, Y. Djamour, A. Walpersdorf et al. (2007). Large-scale velocity field and strain tensor in Iran inferred from GPS measurements: new insight for the present-day deformation pattern within NE Iran, Geophys. J. Int., 170, 436-440.

Mirzaei, N., M. Gao and Y. T. Chen (1998). Seismic sources regionalization for seismic zoning major Seismotectonic provinces, J. Earthquake Pred. Res., 7, 465-495.

Mortezanejad, G., H. Rahimi, F. Romanelli and G. F. Panza (2019). Lateral variation of crust and upper mantle structures in NW Iran derived from surface wave analysis, J. Seismol., 23, 77-108, doi:10.1007/s10950-018-9794-1.

Motaghi, K., M. Tatar and K. Priestley (2012). Crustal thickness variation across the northeast Iran continental collision zone from teleseismic converted waves, J. Seismol, 16, 253-260.

Motaghi, K., M. Tatar, K. Priestley, F. Romanelli et al. (2014). The deep structure of the Iranian Plateau, Gondwana Research, 28, 1, 407-418, doi:10.1016/j.gr.2014.04.009.

Nowrouzi, G., K. F. Priestley, M. Ghafory-Ashtiany, G. J. Doloei et al. (2007). Crustal velocity structure in Iranian Kopeh-Dagh, from analysis of P-waveform receiver functions, J. Seismol, Earthquake Eng., 8, 187-194.

Owens, T. J., G. Zandt and S. R. Taylor (1984). Seismic evidence for an ancient rift beneath the Cumberland Plateau, Tennessee: A detailed analysis of broadband teleseismic P waveforms, J. Geophys. Res., 89, 7783-7795.

Rahimi, H., H. Hamzehloo, F. Vaccari and G. F. Panza (2014). Shear-Wave Velocity Tomography of the Lithosphere-Asthenosphere System beneath the Iranian Plateau, Bull. Seismol. Soc. Am., 104, 6, 2782-2798.

Roostaee, F., H. Rahimi and M. Rastgoo (2021). Determination of crustal velocity structure of NE Iran from local earthquakes travel time inversion, J. Res. Appl. Geophys. (JRAG), 7, 1, 123-134.

Sengor, A. M. C. (1984). The Cimmerides Orogenic System and the Tectonics of Eurasia, Geological Society of America Special Paper, 195, 1-82.

Sengor, A. M. C., D. Altiner, A. Cin, T. Ustaomer et al. (1988). Origin and assembly of the Tethyside ororgenic collage at the expense of Gondowana-Land, M.G. Audley-Charles, A. Hallam (Eds.), Gondwana and Tethys, Geological Society, London, Special Publication, 37, 119-181.

Shabanian, E., O. Bellier, L. Siame, N. Arnaud et al. (2009a). New tectonic configuration in Ne Iran: active strike-slip faulting between the Kopeh Dagh and Binalud mountains, Tectonics, 28, doi:10.1029/2008TC002444.

Shabanian, E., L. Siame, O. Bellier, L. Benedetti et al. (2009b), Quaternary slip rates along the north-eastern boundary of the Arabia-Eurasia collision zone (Kopeh Dagh Mountains, Northeast Iran), Geophys. J. Int., 178, 1055-1077, doi:10.1111/j.1365-246X.2009.04183.x.

Shadmanaman, N. and H. Shomali (2010). Upper mantle S-velocity structure and Moho depth variations across Zagros belt, Arabian-Eurasian plate boundary, Phys. Earth planet. Inter., 180, 92-103.

Sheehan, A. F., G. A. Abers, A. L. Lerner-Lam and C. H. Jones (1995). Crustal thickness variations across the Rocky Mountain Front from teleseismic receiver functions, J. Geophys. Res., 100, B10, 20391-20404.

Sodoudi, F. (2005). Lithospheric structure of the Aegean obtained from P and S receiver functions, PhD thesis, Erstgutachter: Prof. Dr. Rainer Kind, Zweitgutachter: Prof. Dr. Serge Shapiro, Department of Earth Sciences, Freie Universität Berlin, Germany.

Soffel, H. C., M. Davoudzadeh, C. Rolf and S. Schmidt (1996). New palaeomagnetic data from Central Iran and a Triassic palaeoreconstruction, Geologische Rundschau, 85, 293-302.

Stocklin, J. and M. H. Nabavi (1973). Tectonic Map of Iran, 1:2500000. Tehran: Geological Survey of Iran.

Stampfli, G. M., G. D. Borel, W. Cavazza, J. Mosar et al. (2001). Palaeotectonic and palaeogeographic evolution of the western Tethys and PeriTethyan domain (IGCP Project 369), Episodes, 2, 4, 222-228, doi:10.18814/epiiugs/2001/v24i4/001.

Stocklin, J. and M. H. Nabavi (1973). Tectonic Map of Iran 1:2,500,000. Geological Survey of Iran.

Tadayon, M., F. Rossetti, M. Zattin, G. Calzolari, R. Nozaem, F. Salvini, C. Faccenna, P. Khodabakhshi (2019). The long-term evolution of the Doruneh fault region (Central Iran): A key to understanding the spatio-temporal tectonic evolution in the hinterland of the Zagros convergence zone, Geological Journal, 54, 3, 1454-1479.

Taghizadeh-Farahmand, F., F. Sodoudi, N. Afsari and N. Mohammadi (2013). A detailed receiver function image of the lithosphere beneath the Kopeh Dagh (Northeast Iran), J. Seismol., 17, 1207-1221.

Tirrul, R., I. R. Bell, R. J. Griffis and V. E. Camp (1983). The sistan suture zone of eastern Iran, Geol. Soc. Am. Bull., 94, 134-50.

Vernant, P., F. Nilforoushan, D. Hatzfeld, M. R. Abbassi et al. (2004). Present-day crustal deformation and plate kinematics in the Middle East constrained by GPS measurements in Iran and Northern Oman, Geophys. J. Int., 157, 1, 381-398.

Vinnik, L. P. (1977). Detection of waves converted from P to SV in the mantle, Phys. Earth Planet. Int., 15, 1, 39-45.

Wellman, H. W. (1965). Active wrench faults of Iran, Afghanistan and Pakistan, Geologische Rundschau, 18, 217-34.

Yanovskaya, T. B. and P. G. Ditmar (1990). Smoothness criteria in surface wave tomography, Geophys. J. Int., 102, 63-72.

Yanovskaya, T. B. (1997). Resolution estimation in the problems of seismic ray tomography, Izvestiya, Phys. Solid Earth, 33, 9, 762-765.

Yanovskaya, T. B., E. S. Kizima and L. M. Antonova (1998). Structure of the crust in the Black Sea and adjoining regions from surface wave data, J. Seismol., 2, 4, 303-316, doi:10.1023/A:1009716017960.

Zhu, L. P. and H. Kanamori (2000). Moho depth variation in southern California from teleseismic receiver functions, J. Geophys. Res., 105, 2969-2980.

Zonenshain, L. P., M. I. Kuzmin and L. M. Natapov (1990). Geology of the USSR: A Plate-Tectonic Synthesis, 242, AGU, Washington, D. C.

***CORRESPONDING AUTHOR: Habib RAHIMI**,
Institute of Geophysics, University of Tehran, Tehran, Iran
e-mail: rahimih@ut.ac.ir